International Journal of Nanomedicine

Dovepress
Taylor & Francis Group

Open Access Full Text Article

ORIGINAL RESEARCH

# Dendritic Cell Repression by TNF-α-Primed Exosomes Accelerate T2DM Wound Healing Through miR-146a-5p/TXNIP/NLRP3 Axis

Jiaqi Li[1–3,*], Xiaoxuan Lin[4,*], Jinyang Wang[1–3,*], Xuanyi Li[1–3], Zhengchuan Zhang[1,2], Leyang Ji[1–3], Rongcheng Yu[1–3], Xiaoxing Kou[1–3], Yang Yang[1,2]

[1]Hospital of Stomatology, Guanghua School of Stomatology, Sun Yat-Sen University, Guangzhou, 510055, People's Republic of China; [2]Guangdong Provincial Key Laboratory of Stomatology, Guangzhou, 510055, People's Republic of China; [3]South China Center of Craniofacial Stem Cell Research, Guanghua School of Stomatology, Sun Yat-Sen University, Guangzhou, 510055, People's Republic of China; [4]Department of Stomatology, The Fifth Affiliated Hospital of Sun Yat-Sen University, Zhuhai, 519000, People's Republic of China

*These authors contributed equally to this work

Correspondence: Xiaoxing Kou; Yang Yang, Department of Oral Implantology, Hospital of Stomatology, Guanghua School of Stomatology, Sun Yat-sen University, No. 56 of LingYuanXiLu, Guangzhou, Guangdong, 510055, People's Republic of China, Email kouxiaoxing@mail.sysu.edu.cn; yangy855@mail.sysu.edu.cn

**Introduction:** Type 2 diabetes mellitus (T2DM) impairs wound healing due to hyperglycemia-induced immune dysfunction. Dendritic cells (DCs) in the skin are crucial for wound healing but are adversely affected by hyperglycemic microenvironment. Exosomes derived from mesenchymal stem cells (MSC-exos), especially adipose-derived MSCs (ADSCs) with higher accessibility, have shown potential for immune regulation. However, their yield and efficacy can be limited. This study aims to explore the effects of TNF-α-preconditioned ADSCs-exos (T-exos) on restoring DC function and accelerating wound healing in T2DM.

**Methods:** T-exos were isolated from ADSCs pretreated with TNF-α. The regulatory effects of T-exos on DC immune responses under high glucose conditions were assessed. Subsequently, the roles of DCs treated with T-exos in diabetic wound healing were evaluated. Finally, the mechanism underlying T-exos-mediated regulation of DCs was investigated in detail.

**Results:** Under high glucose conditions, T-exos suppressed DC activation, as evidenced by reduced CD80/CD86 expression and NLRP3 inflammasome activity. In vivo studies showed that T-exos promoted wound closure in T2DM mice, enhancing collagen deposition, angiogenesis, and fibroblast proliferation. Mechanistically, TNF-α enriched miR-146a-5p in exosomes, which targeted TXNIP to inhibit NLRP3 inflammasome activation in DCs. Knockdown of miR-146a-5p abolished these effects in vitro and the therapeutic effect of T-exos on wound healing in vivo.

**Conclusion:** This study elucidates a previously unrecognized role for T-exos in effectively regulating DC activation through the miR-146a-5p/TXINP/NLRP3 axis, which in turn modulates the NLRP3 inflammasome pathway. By synergistically dampening inflammation and enhancing tissue repair, T-exos exhibit significant potential for clinical application in T2DM wounds.

**Keywords:** diabetic wounds, TNF-α-primed exosomes, dendritic cells, NLRP3 inflammasome, miR-146a-5p

## Introduction

Type 2 diabetes mellitus (T2DM), characterized by insulin resistance and pancreatic β cell dysfunction, is a complicated metabolic disorder marked by chronic hyperglycemia.[1] Currently, over 537 million adults worldwide are affected by diabetes, with impaired wound healing contributing significantly to morbidity and mortality.[2,3] Among the various complications, impaired wound healing remains a critical clinical challenge, even causing serious issues such as diabetes foot ulcers.[4] In T2DM, hyperglycemia disrupts the regulated physiological process of wound repair by inducing chronic inflammation and microbial overgrowth.[5–7] The hyperglycemic microenvironment also impairs neovascularization while suppressing stem cell activation.[8,9] More importantly, the breakdown in immune-stromal cell communication further

Received: 20 March 2025
Accepted: 30 July 2025
Published: 15 August 2025

## Graphical Abstract

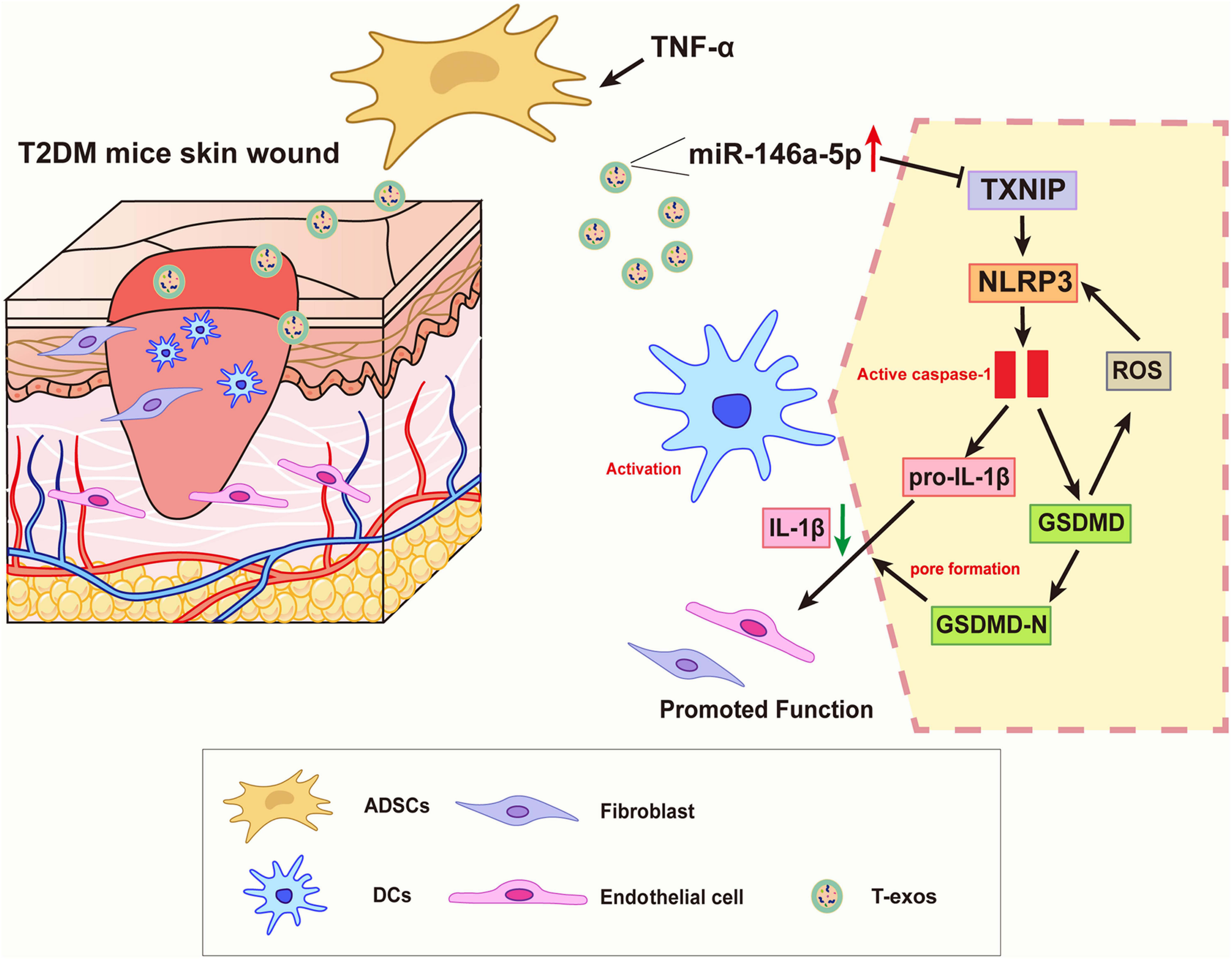

exacerbates tissue repair.[10,11] Notably, immune dysregulation in T2DM extends beyond macrophages and T-cells to dendritic cells (DCs), which are pivotal in bridging innate and adaptive immunity but remain understudied in diabetic wounds.[12–14] Therefore, it is imperative to explore more effective therapies for accelerating T2DM wound healing and improving patients' life quality.

DCs are abundant in the skin and play a crucial role in immune surveillance, antigen presentation, and inflammation resolution, ensuring a timely transition from proinflammatory to tissue-repair phases.[15,16] However, T2DM hyperglycemia induces DC immune dysfunction, marked by upregulating co-stimulatory markers and compromising immune functions.[17,18] These not only weaken the host's immune functions but also disrupt the crosstalk between immune cells and tissue regeneration.[19,20] Recently, studies demonstrated that DCs were important in controlling wound healing processes, and the dysfunction of DCs in T2DM significantly weaken the alleviation of DC-mediated inflammation and led to delayed wound healing.[21,22] Therefore, managing DC immune behavior to neutralize the unfavorable immune environment was a key point to promote wound healing in T2DM conditions.

Mesenchymal stem cell (MSC)-derived exosomes (MSC-exos) have emerged as a crucial carriers for delivering miRNAs, proteins, and lipids to regulate immune cells and promote tissue regeneration, which become an alternative treatment for various diseases, including T2DM.[23–29] However, native MSCs-exos often exhibit limited cargo loading of active components and the high cost of acquisition, which leading to hinder further clinical application in pathologic condition such as T2DM.[30] Preconditioning MSCs with inflammatory cytokines, such as TNF-α, has enhanced exosome yield and enriched miRNAs and proteins.[31,32] Recent study indicated that TNF-α-primed MSC-exos (T-exos) promote M2 macrophage polarization and bone repair in periodontitis, indicating their immunomodulatory potential.[32] Adipose-derived stromal cells (ADSCs), a subset of MSCs, are highly advantageous in clinical applications due to their abundant availability, robust proliferative capacity, and potent paracrine and immunomodulatory functions mediated by their unique secretome.[33,34] Therefore, ADSC can serve as an ideal donor for T-exos.

Despite these advances, the role of T-exos in rectifying DC dysfunction during diabetic wound healing and the underlying mechanisms remain unclear. In this study, we investigated the regulatory effect of T-exos on the immune status of DCs around T2DM wounds, as well as their impact on wound healing, and explored the relevant mechanisms. Our findings establish T-exos as a novel nanotherapeutic strategy for diabetic wounds, bridging immune modulation and tissue regeneration through DC-targeted exosome engineering.

# Materials and Methods

## Animals and Cell Culture

C57BL/6J mice were purchased from the Laboratory Animal Center of Sun Yat-Sen University. All procedures were conducted following the protocols approved by the Institutional Animal Care and Use Committee at Sun Yat-sen University (SYSU-IACUC-2023-000078).

For murine ADSCs isolation, male C57BL/6 mice aged 2 weeks bought from Sun Yat-Sen University laboratory animal center were used in this study. Briefly, the inguinal subcutaneous adipose tissue was collected and cut into pieces. The adipose tissues were enzymatically digested by incubation at 37 °C for 1 h in phosphate-buffered saline (PBS) supplemented with 2 mg/mL collagenase type I (Worthington Biochemical, USA) and 4 mg/mL dispase II (Roche, Switzerland). Then cells were resuspended in α-MEM (Gibco, USA) containing 15% FBS (Gibco, USA), and 100 U/mL penicillin/streptomycin (Gibco, USA), and passaged at 80% density. The ADSCs between passages 3 and 5 were utilized for subsequent experiments.

The murine DC line, mouse endothelial cell line bEnd.3, and fibroblasts cell line NIH-3T3 (Service Bio, China) were cultured with low-glucose DMEM (5.5 mM glucose) containing 10% FBS and 100 U/mL penicillin/streptomycin before using and passaged at 80% density. For high-glucose (HG) conditions, cells were cultured with high-glucose DMEM (35 mM glucose).

## TNF-α Priming Exosome Isolation and Characterization

The ADSCs were cultured in serum-free medium with or without 30 ng/mL TNF-α (Peprotech, USA) for 24 h, then the serums were collected and successively centrifuged 600 g for 10 min and 3000 g for 10 min to remove cell debris and centrifuged at 10000 g for 30 min to remove the impurity. Next, the supernatant was centrifuged at 120000 g for 120 min, the pellet was C-exos or T-exos.

For exosome characterization, the diameter and quantity of exosomes were measured by nanoparticle tracking analysis (NTA) (ZetaView PMX120, Germany). Data were analyzed using the ZetaView. The morphology of exosomes was observed with transmission electronic microscopy (TEM) analysis. Identification of surface markers was validated by nanoflow cytometry (NanoFCM, China).

## T2DM Induction

For T2DM induction, C57BL/6J mice (4-week age) were fed a high-fat diets (60% kcal fat; Research Diets) for 2 months and then kept empty stomach for 12 h before STZ injection. The 1% STZ diluted in PH 2.1 citrate buffer solution was prepared and then injected intraperitoneally with a dose of 120 mg/100 g. Successful establishment of the T2DM mouse model was confirmed by assessing two key criteria: (1) Significant body weight gain (≥ 15% increase compared to non-induced mice) observed during the high-fat diet and low-dose streptozotocin induction period and (2) Fasting blood glucose levels exceeding 11.1 mmol/L in two consecutive measurements after overnight fasting.[35] The mice that unsuccessfully made suffered a secondary injection of 50 mg STZ to induce T2DM.

## Animal Skin Wound Model and Treatment

T2DM mice were used to create the skin wound healing models (n = 5). After the mice were anesthetized and the dorsal skin was shaved using a mechanical trimmer with depilatory cream, a 1 cm x 1 cm square-shaped wound was created. To assess the capacity of different exosomes to impact skin wound repair, the mice were randomly allocated into PBS, C-exos, and T-exos groups. Exosomes resuspended in PBS (100 μg dissolved in 80 μL PBS) were locally administered subcutaneously around wounds at 4 injection sites after surgery. The percentage of wound closure was quantified on photographs using ImageJ software. To minimize bias, wound images were coded and analyzed by two independent researchers unaware of the experimental groups, with closure rate calculated as (initial area - current area)/initial area × 100%. Three or fourteen days after surgery, mice were sacrificed and skin samples were harvested for immunofluorescent staining or histological staining, respectively.

## Subcutaneous Injections of Exosomes

Subcutaneous injections were performed using ultra-fine insulin needles to deliver exosomes. The skin was gently lifted to form a tent, and the needle was inserted through the epidermis into the underlying loose connective tissue. A 10–20 μL volume of the exosome suspension was administered at each injection site around the wound. This caused a minor raised area in the skin without migration or leakage. Subcutaneous exosomes were absorbed within 0.5–2 hours.

## Exosome Tracing in vivo

Exosomes were labeled with PKH26 (Merck, Germany) according to the manufacturer's instructions and collected by ultra-centrifugation. Subsequently, $1*10^8$ PKH26 labeled exosomes were administered subcutaneously near the skin wounds of T2DM mice. Skin tissue samples were collected 24 h after exosome administration, followed by fixation and dehydration processes in preparation for frozen sectioning. Images were captured with Zeiss LSM 900 confocal microscope and analyzed using ImageJ software.

## Histological Staining

Following euthanasia, skin wound specimens were immediately fixed in 4% paraformaldehyde at 4°C for 24 h. Tissue samples collected at the 14-day time point were subsequently processed by a graded ethanol series for dehydration, followed by paraffin embedding. Histological analysis was performed using Hematoxylin and Eosin (H&E) (Solarbio, China) and Masson's trichrome staining kits (Solarbio, China) according to the manufacturer's protocols. The images were captured by a Leica Aperio AT2 microscope and analyzed using ImageJ software. The 3 days' samples were fixed and dehydrated for frozen sectioning and immunofluorescent staining.

## Quantitative Real Time PCR (qRT-PCR) Analysis

For qRT-PCR analysis, the total RNA of cells or exosomes were extracted utilizing RNA-Quick Purification Kit (Yishan, China) according to the instructions. The extracted cell mRNA was reverse transcribed with the RT Master Mix (Takara, Japan), and the exosome miRNA was reverse transcribed with the miRNA 1st strand cDNA synthesis kit (AG, China). Then the expression of object genes was detected on a LightCycler96 (Roche, Switzerland) with LightCycler 480 SYBR Green I Master Mix (Roche, Switzerland). The mean cycle threshold (Ct) values were normalized against β-actin. The Ct method was applied to calculate the fold change compared to the control group. The primer sequences were supplied in Table S1, and the reagents and antibodies used in this study were shown in Table S2.

## Western Blots Analysis

For Western blots, the total proteins were harvested by lysing cells or exosomes on ice with a mixture of RIPA with protease inhibitor and phosphatase inhibitor cocktail (Beyotime, China). Then, samples were centrifuged at 12000 g for 15 min after sonication. The supernatant was collected, and the protein concentration was determined utilizing a bicinchoninic acid assay kit (Cwbio, China). 20 μg of proteins were separated on SDS-PAGE gels and transferred onto a polyvinylidene difluoride membrane (Merck, Germany). The membranes were blocked with 5% BSA in tris buffered saline with tween (TBST) for 1 h, followed by incubating on the primary antibody (1:1000 dilution) at 4 ˚C overnight. Then, the membranes were treated with the HRP-conjugated secondary antibodies (Biosharp, China) for 1 h at room temperature. The membranes were incubated with Immobilon Chemiluminescent HRP substrate (Merck, Germany), and the protein bands were visualized with the chemiluminescence imaging system (Bio-Rad, USA). Primary antibodies were specific for CD9, TSG101, IL-1β, SMPD3 (Abcam, UK), CD63 (Santa Cruz, USA), Rab27A, Rab27B, GSDMD (Affinity, China), SMPD3, NLRP3, TXNIP, β-actin (Abclonal, China).

## The Intake of Exosomes

Exosomes were labeled with PKH26 and collected by ultra-centrifugation. PKH26 labeled exosomes were co-cultured with DCs in high-glucose conditions in 24-well dish. After 12 h of incubation, cells were fixed with 4% PFA and blocked with 1% BSA for 60 min, followed by staining with Cell mask (Invitrogen, USA) for 10 min and DAPI for 2 min under dark conditions. The images were captured by a Zeiss LSM 900 confocal microscope and analyzed using ImageJ software.

## Immunofluorescent Staining

For immunofluorescence staining, cells were seeded in 24-well plates and treated according to the experimental design. Samples were fixed with 4% PFA and permeabilized with 0.3% Triton X-100, and then blocked with 5% BSA for 60 min. Samples were incubated with primary antibodies overnight at 4 ˚C, and then incubated with secondary antibodies for 1 h at room temperature. Cell membrane and cytoskeleton were stained by WGA (MKbio, China) and Phalloidin (Invitrogen, USA) for 10–15 min. Cell nuclei were colored with DAPI (Abcam, UK). For tissue immunofluorescence staining, frozen sections were washed in PBS three times and then blocked in 5% BSA with 0.3% triton for 60 min at room temperature. Then sections were incubated with primary antibodies overnight, followed by incubation with secondary antibodies. The images were captured by a Zeiss LSM 900 confocal microscope and analyzed using ImageJ software. Primary antibodies, CD80 (Biolegend, USA), Cl-GSDMD (CST, USA), Cl-Caspase1, Ki67a (Affinity, China), a-SMA, CD31 (Abclonal, China), NLRP3 (Abclonal, China) were used in this study.

## Flow Cytometry Analysis

For DC activation detection, cells were collected by non-EDTA trypsin and washed twice with PBS. After resuspended in PBS containing 2% bovine serum albumin (BSA), cells were stained with APC-labeled CD86 primary antibody, FITC-labeled CD80 primary antibody (eBioscience, USA) for 1 h. After washing twice, data were acquired with a flow cytometer (CytoFlex, USA) and analyzed. Flow cytometric analysis was also used to detect PE-labeled CD29, CD44, CD45, and CD34 (BioLegend, USA) expression in ADSCs.

## Cell Viability

Cells were seeded at a density of $10^4$ cells per well on 96-well plates to assess their viability after treatment. At each time point, 10% Cell Counting Kit-8 (CCK-8, Dojindo, Japan) solution was added to each well. The plates were incubated for 1 h, and the absorbance at 450 nm was measured utilizing a microplate reader.

## Reactive Oxygen Species (ROS) Detection

To detect ROS, the culture medium of DCs was replaced with a serum-free medium containing DCFH-DA and incubated at 37°C for 15 min. Afterward, the cells were washed three times with PBS and collected following trypsin digestion. ROS activity was measured using the FITC fluorescence channel on a flow cytometer (CytoFlex, USA) and analyzed with CytoExpert.

## Enzyme-Linked Immunosorbent Assay (ELISA)

For detection of inflammatory factor expressions, the DC supernatants were collected, centrifuged at 600 g and then at 12,000 g to remove cell pellets. Cytokine concentrations of IL-1β and IL-18 in 100 μL of supernatant were determined using an ELISA Kit (Cusabio, China), following the manufacturer's instructions.

## Condition Medium (CM) Collecting

DCs were cultured with high glucose complete medium with the addition of PBS or exosomes for 24 h. The culture medium was harvested and centrifuged at 600g and 12000g, to discard the pellets. The supernatant was mixed with high glucose complete medium as the CM for endothelial cells and fibroblasts culture. The CM obtained from DCs treated with T-exos and C-exos were named T-CM and C-CM, respectively.

## Migration Activity Analysis

The wound healing and transwell assays were conducted to evaluate the migration activity of endothelial cells. For wound healing assays, bEnd.3 cells were seeded into 6-well plates and cultured to 90% density. A scratch was created in each well with a 200 ul pipette tip. The images at 0 h and 24 h were photographed with a camera on microscope. The proportion of wound healing areas was calculated with ImageJ. For transwell assays, $10^5$ cells were seeded in transwell chambers with a serum-free medium, and the chambers were placed in 24-well plates containing different CM. After 12 h, cells were fixed with 4% PFA, stained with crystal violet, and images were captured using a microscope. The number of migrated cells was then counted.

## Tube Formation Assays

For tube formation assays, 200 ul Matrigel (Corning, USA) were added into 24-well plate and then incubated at 37°C for 30 min, then $1.5*10^5$ cells were resuspended with different CM and seeded into the wells. After 6 h of incubation, the images of tube formation were captured by microscope and analyzed by ImageJ.

## Small-RNA Sequencing and Data Analysis

Small-RNA sequencing of the C-exos and T-exos was performed using the BGI platform (BGI Genomics, China). The clean reads were then mapped to the reference genome or transcriptome using BGI, and differential expression analysis was performed using DESeq2. The DESeq2 was employed for differential miRNA expression analysis, applying stringent criteria of minimum 2-fold change and a significance level of $p < 0.01$ after multiple testing correction.

The processed target sequences undergo statistical analysis of sequence length distribution and common sequence statistics among samples. The cleaned target sequences were classified and annotated, providing information on the components and expression levels contained in the samples. For identified miRNAs, target gene prediction and GO functional annotation are performed.

## miRNA Transfection

For miR-146a-5p inhibition studies, ADSCs were transfected with specific inhibitors (50 nM working concentration) using the Lipofectamine 3000 system (Invitrogen, USA) in accordance with the manufacturer's guidelines. Negative inhibitors were simultaneously transfected as negative controls to account for potential off-target effects. For inhibitors of miR-146a-5p, ADSCs were transfected with RNA at a final concentration of 50 nM using lipo3000 transfection reagents (Invitrogen, USA) according to the manufacturer's instructions. Negative control inhibitors were transfected to serve as matched controls. The exosomes were collected after transfection according to the protocol mentioned before, and the transfection efficiency of miR-146a-5p was tested by qRT-PCR.

## Dual-Luciferase Reporter Assays

To validate the interaction between TXNIP and miR-146a-5p, we performed dual-luciferase reporter assays. We cloned either the wild-type (WT) or mutant (MUT) sequence of TXNIP into the psiCHECK-2 luciferase vector (Promega, USA). HEK293T cells were co-transfected with the constructs and miR-146a-5p mimics (or negative control mimics) using Lipofectamine 3000 (Invitrogen, USA) following the manufacturer's protocol. 48 h after transfection, luciferase activity was measured using the Dual-Luciferase Reporter Assay System (Promega, USA), the results were normalized to Renilla luciferase activity.

## Statistical Analysis

Unless stated otherwise, data are presented as means ± standard deviations for each group, with experiments repeated at least three times. Statistical differences were assessed using analysis of variance, followed by Bonferroni's multiple comparison test with GraphPad Prism 9 software (San Diego, CA, USA). A p-value of $< 0.05$ was considered statistically significant.

# Results

## Identification of ADSCs and TNF-α-Primed Exosomes

ADSCs were isolated from murine subcutaneous tissue and validated by flow cytometry, which demonstrated that ADSCs highly expressed the positive MSC markers CD29 and CD44 but were negative for hematopoietic cell markers such as CD34 and CD45 (Figure S1). As illustrated in the schematic diagram (Figure 1A), exosomes were isolated from TNF-α-primed ADSCs (T-exos) and untreated controls (C-exos). The morphology of the exosomes was examined using TEM, revealing that both exosomes displayed a typical saucer-like shape with a diameter of approximately 150 nm (Figure 1B). NTA confirmed that both exosomes were similar in size; however, there was a 2.15-fold increase in exosome yield following TNF-α pretreatment (Figure 1C). The nanoflow cytometric and Western blot results demonstrated that T-exos and C-exos expressed similar levels of exosome markers, including CD9, CD63, CD81, and TSG101 (Figure 1D and E). Then, we further evaluated the exosome secretion by analyzing the expression levels of Rab27A, Rab27B and SMPD3. We found that TNF-α stimulation upregulated both the mRNA and protein expression of Rab27A, Rab27B and SMPD3 (Figure 1F and G), indicating enhanced exosome biogenesis. Exosomes transfer miRNA to facilitate intercellular communication through transcriptional regulation. To reveal the miRNA expression profiles in exosomes derived from TNF-α-pretreated ADSCs, we conducted miRNA sequencing. Venn analysis indicated that 388 miRNAs were commonly presented in C-exos and T-exos. Furthermore, miRNA sequencing identified 105 miRNAs that were uniquely enriched in T-exos (Figure 1H). GO annotation analysis highlighted the involvement of these miRNA target genes in infectious disease, the immune system, and the regulation of inflammatory pathways (Figure 1I). Overall, the results imply that TNF-α pretreatment not only enhanced the secretion of exosomes from ADSCs but also significantly altered the miRNA profiles within those exosomes.

## T-Exos Suppress DC Activation Under HG Conditions

DCs are widely spread in skin tissues and play a significant role in maintaining skin immune homeostasis.[16] We compared the distribution of activated DCs in the skin of normal and T2DM mice. Our findings showed that a higher number of activated DCs were distributed in the dermis as well as in the sub-dermis of the skin in T2DM mice (Figure 2A). Next, 35 mM of glucose was applied in cell culture medium for mimicking HG environment in T2DM mice. Immunofluorescence staining indicated that the morphology of DCs presents an activated state, which displayed irregular morphology with extended processes and branched structures in HG conditions (Figure 2B). The flow cytometry analysis and qRT-PCR showed a significant increase of the activation-related genes CD80, CD86, and MHC-II expression level in DCs cultured in HG conditions (Figure 2C–E). Then, we explored the therapeutic effects of T-exos on DC immune dysfunction under HG conditions, C-exos and PBS were set as compared groups. The immune-fluorescence images revealed the presence of PKH26-labeled exosomes within the cytoplasm of DCs after 12 h of culture (Figure 2F). Flow cytometry analysis further confirmed that exosomes were successfully taken up by DCs. (Figure S2A), without significant differences between C-exos and T-exos groups (Figure S2B). CCK-8 results showed that the viability of DCs in the exosome-treated groups was higher than that in the control group, with no significant differences observed between C-exos and T-exos groups (Figure S2C). The immunofluorescence images indicated that DCs cultured with T-exos exhibited relatively uniform morphology, with the shortest extended processes and the largest cytoplasm /nuclear

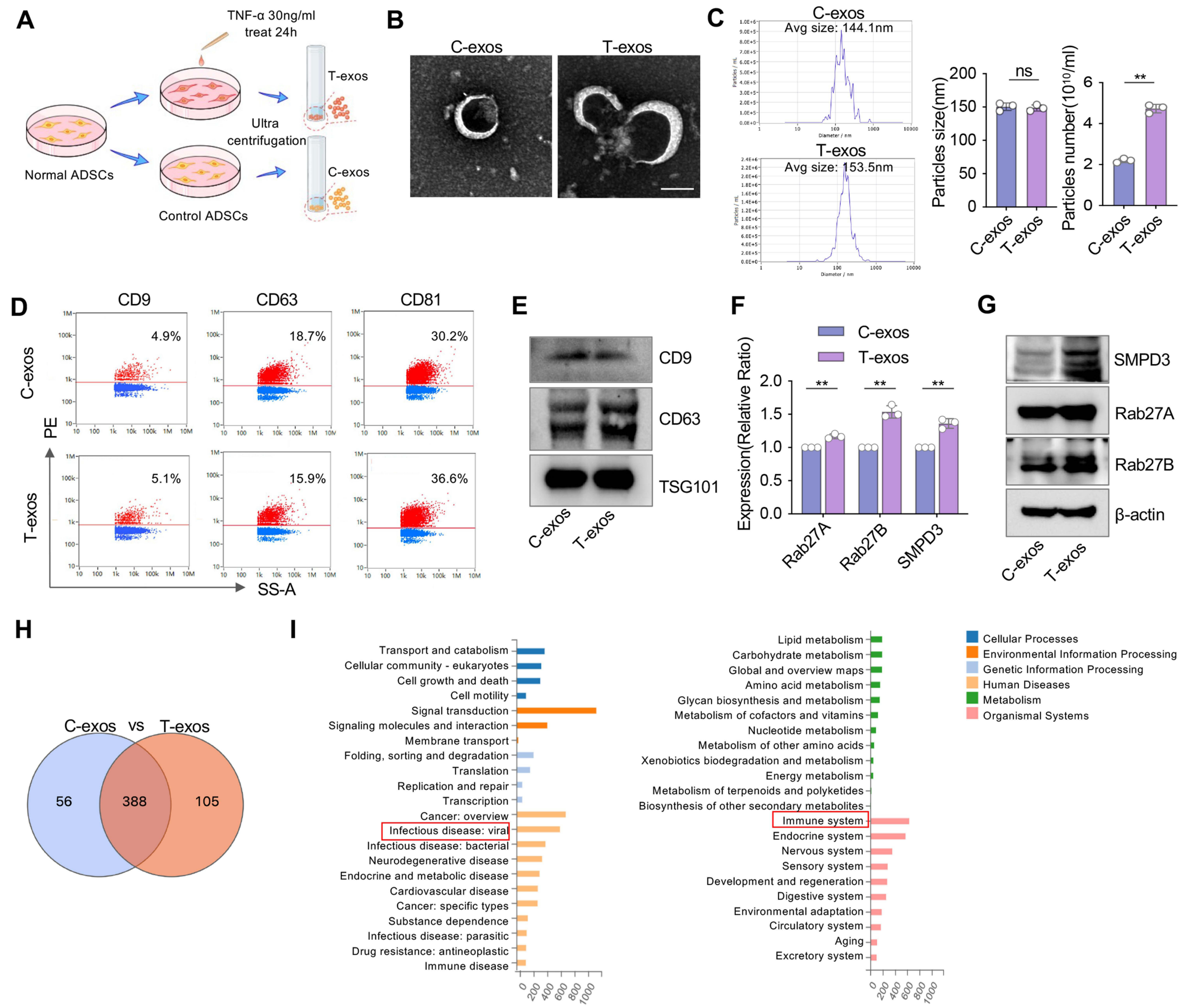

**Figure 1** Characterization of exosomes from TNF-α pretreated ADSCs. (**A**) Schematic illustrating the ADSCs pretreatment and exosome isolation. ADSCs were exposed to 30 ng/mL TNF-α for 24 hours, then exosomes were isolated using an ultracentrifuge system. (**B**) Representative TEM images show the morphology of C-exos and T-exos. Scale bar = 100 nm. (**C**) Particles size distribution analysis and particles number per milliliter of C-exos and T-exos using NTA. (n = 3). (**D** and **E**) Nanoflow cytometry and Western blots analysis of CD9, CD63, CD81, and TSG101 in C-exos and T-exos. (**F**) The relative mRNA expression levels of SMPD3, Rab27A, and Rab27B in C-exos and T-exos were determined by qRT-PCR. (**G**) Western blots analysis of SMPD3, Rab27A, and Rab27B in C-exos and T-exos. (**H**) Venn diagram shows the overlap of identified miRNA between C-exos and T-exos. (**I**) The analysis of GO database annotation revealed that the differentially expressed miRNAs are associated with immune diseases and inflammatory pathways. Data are presented as mean ± SD (n = 3). ns, not significant. $^{**}P < 0.01$.

area ratio. (Figures 2G, H and S2D). The flow cytometry analysis and qRT-PCR analysis revealed that the T-exos group exhibited the lowest expression of CD80 and CD86, with the tendency T-exos < C-exos < HG (Figures 2I–K, S2E and F). These results suggest that T-exos can inhibit the activation of DCs in HG conditions, exhibiting more prominent regulatory effects compared to C-exos.

## T-Exos Enhance Fibroblast and Endothelial Cell Activities via DC Modulation

The wound healing process post-injury includes the germination of blood vessels and extracellular matrix synthesis, which are deeply controlled by local immune microenvironments. Diabetic patients suffer from a state of low-grade chronic inflammation, which leads to poor microvascular circulation and impaired collagen synthesis. To investigate the regulatory capacity of DCs on fibroblasts and endothelial cell functions, we used different CMs as the culture mediums of bEnd.3 and NIH-3T3 cell line (Figure 3A). CCK-8 assays showed that fibroblasts and endothelial cells treated with

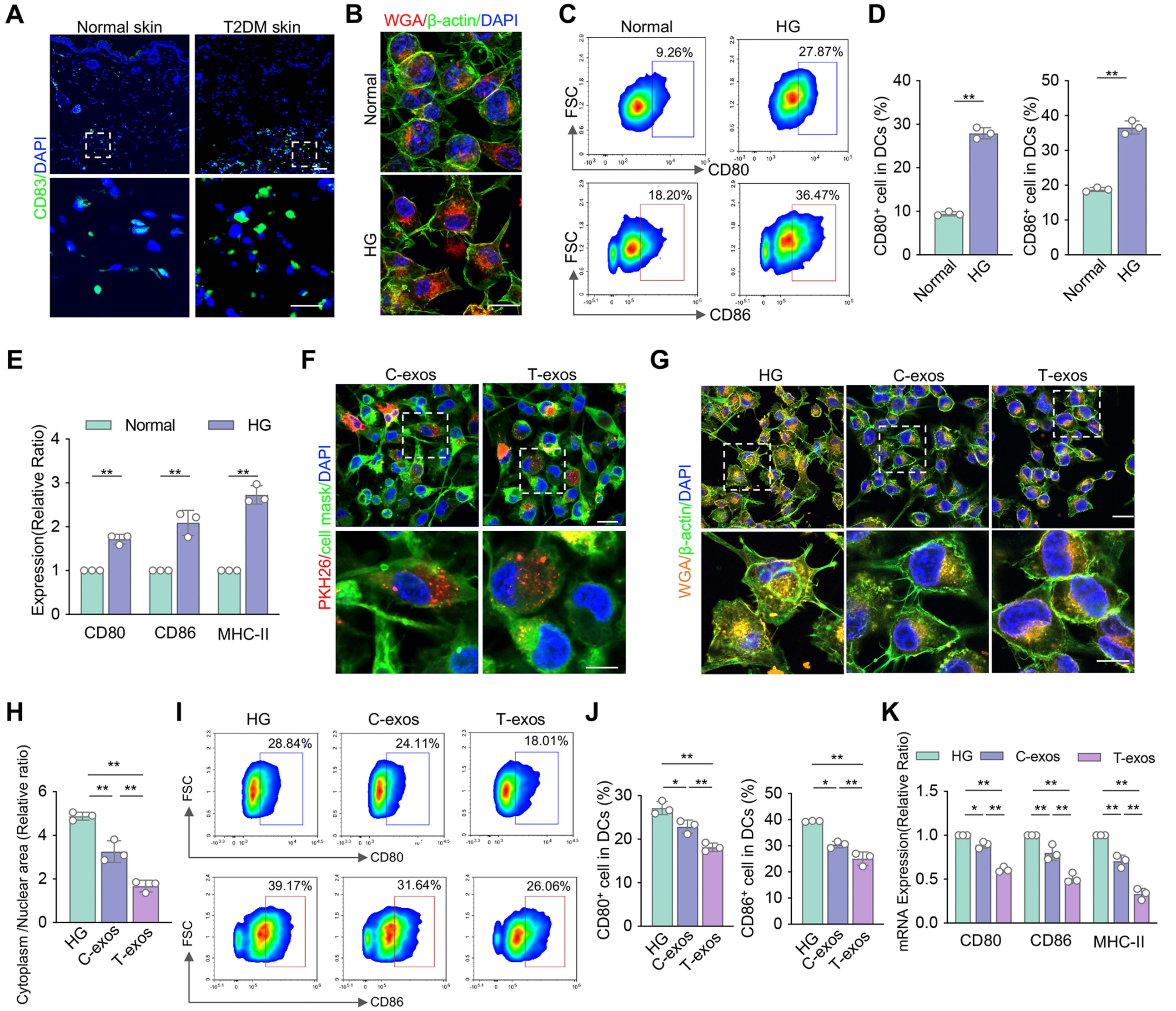

**Figure 2** T-exos significantly impede the activation of DCs in high-glucose conditions. (**A**) Immunofluorescent images show the distribution of CD83$^+$ cells in skin from normal mice and T2DM mice, respectively. Scale bar = 50 μm (up), 20 μm (down). (**B**) The morphology of DCs was demonstrated via laser scanning confocal microscopy, the cytoskeleton, cell membrane, and cell nucleus were stained green, red, and blue, respectively. Scale bar = 10 μm. (**C** and **D**) The flow cytometry analysis shows the relative expression of CD80 and CD86 in normal-cultured DCs and HG-cultured DCs. (**E**) The relative mRNA expression levels of CD80, CD86, and MHC-II in DCs cultured by normal medium and HG medium were tested by qRT-PCR. (**F**) The uptake of PKH26-labeled C-exos and T-exos in DCs were visualized by fluorescence microscope. The exosomes, cell membrane, and cell nucleus were stained red, green, and blue, respectively. Scale bar = 10 μm (up), 5 μm (down). (**G**) Representative immuno-fluorescence images of DCs co-culture with C-exos and T-exos in high-glucose conditions. The cell membrane was stained with WGA (red), and the cytoskeleton was stained green. Scale bar = 10 μm (up), 5 μm (down). (**H**) The relative ratio of cytoplasm/nuclear area to represent the activation status of DCs was measured. (**I**–**K**) The relative expression levels of CD80, CD86, and MHC-II in DCs treated by C-exos and T-exos were examined by flow cytometry analysis and qRT-PCR. Data are presented as mean ± SD (n = 3). ns, not significant. $*P < 0.05$, $**P < 0.01$.

T-CM had the highest cell viability, while the C-CM group also exhibited relatively higher cell viability compared to the control group (Figure S3A and B). The qRT-PCR and Western blot assay results showed that T-CM group expressed the highest COL1A1, COL3A1, α-SMA, and FN-1, while the C-CM group showed the opposite trend (Figure 3B and E). Immunofluorescence staining was performed to evaluate Ki67-positive cells in fibroblasts stimulated with different CMs. The results showed that T-CM group exhibited the highest cell proliferation activity compared to the other groups (Figure 3C and D). Furthermore, we observed that angiogenesis-related genes in bEnd.3 cells, such as CD31, ANG-1, vWF, and KDR, were expressed significantly higher in the T-CM group compared to the other groups (Figure 3F). Wound healing and transwell assays were performed to assess the migration capacity of bEnd.3 cells. The results revealed that T-CM group had superior migration capacity compared to the other groups, while control group showed the

https://doi.org/10.2147/IJN.S522994

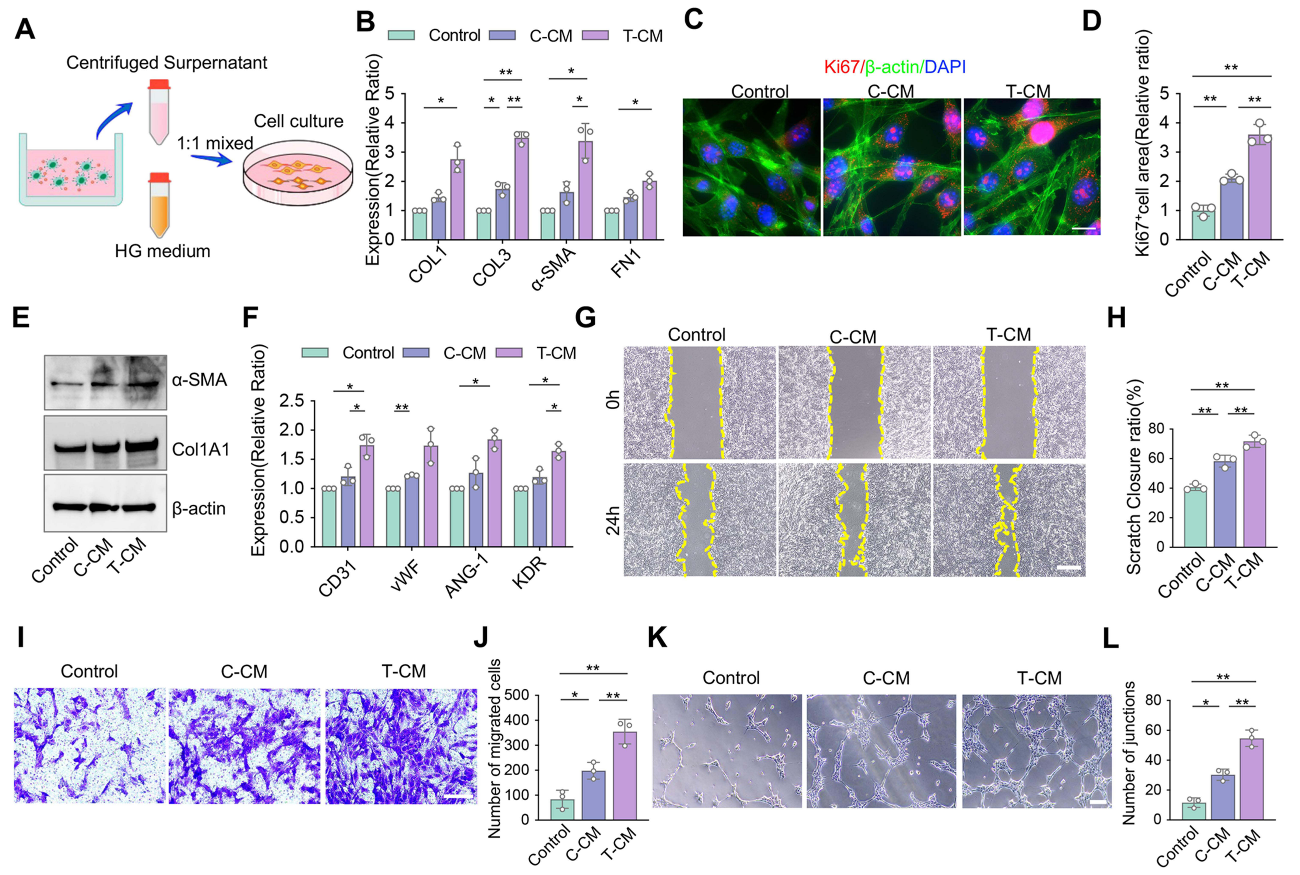

**Figure 3** Co-culture of DCs with T-exos promote fibrogenesis and angiogenesis under high-glucose conditions. (**A**) Schematic diagram of co-culturing NIH-3T3/Bend.3 cells with DCs treated by C-exos or T-exos. (**B**) The gene expression levels of COL1, COL3, α-SMA, and FN-1 in NIH-3T3 cells were determined by qRT-PCR. (**C** and **D**) The immunofluorescent staining and quantification of Ki67 (red) in NIH-3T3 cells co-culture with differently treated CM. Scale bar = 5 μm. (**E**) The Western blots images of α-SMA and Col1A1 in NIH-3T3 treated with different CM. (**F**) The gene expression levels of CD31, vWF, ANG-1, and KDR in bEnd.3 determined by qRT-PCR. (**G** and **H**) The wound healing assay of bEnd.3 and the wound closure rate were counted. Scale bar = 500 μm. (**I** and **J**) Transwell assay was used to assess the cell migration capacity of bEnd.3, and the number of migrated cells was counted. Scale bar = 50 μm. (**K** and **L**) Tube formation assay was performed to visualize the cell capillary network formation of bEnd.3, and the number of junctions was counted. Scale bar = 50 μm. Data are presented as mean ± SD (n = 3). ns, not significant. $^{*}P < 0.05$, $^{**}P < 0.01$.

weakest cell migration rate (Figure 3G–J). Tube formation assays showed that endothelial cells treated with T-CM formed a significantly higher number of tube junctions, suggesting an enhanced pro-angiogenic potential (Figure 3K and L). Overall, the T-CM group appeared to significantly boost the fibroblasts and endothelial cells functions in HG conditions. This indicate that T-exos may play a crucial role in accelerating the wound healing process by influencing DC immune responses in T2DM conditions.

## T-Exos Inhibit DC Activation and Promote Wound Healing in T2DM Mice

To assess the in vivo performances of the T-exos, we injected different exosomes around the wounds in the skin of T2DM mice, PBS was used as negative control. When equal numbers of C-exos and T-exos were infused, T-exos groups showed significantly accelerated wound healing compared to C-exos and PBS groups post-wound creations (Figure 4A–C). H&E and Masson staining confirmed that the T-exos group exhibited the highest ratio of newly formed collagen and granulation tissue maturity around the wounds, while the PBS group showed a minimal ratio of new collagen and epithelium formation (Figures 4D, S4A and B). In the immunofluorescence staining images, more CD31 and α-SMA positive cells were detected in the T-exos group at the interface under the wounds than in other groups, which indicated T-exos promoted endothelial cell and fibroblasts activities during tissue repairing (Figure 4E–G). These results suggest that T-exos exhibit superior in vivo therapeutic effects in promoting wound healing in T2DM mice. Subsequently, we have compared with T-exos and C-exos in non-diabetic C57BL/6 mice models. The results showed that both C-exos and

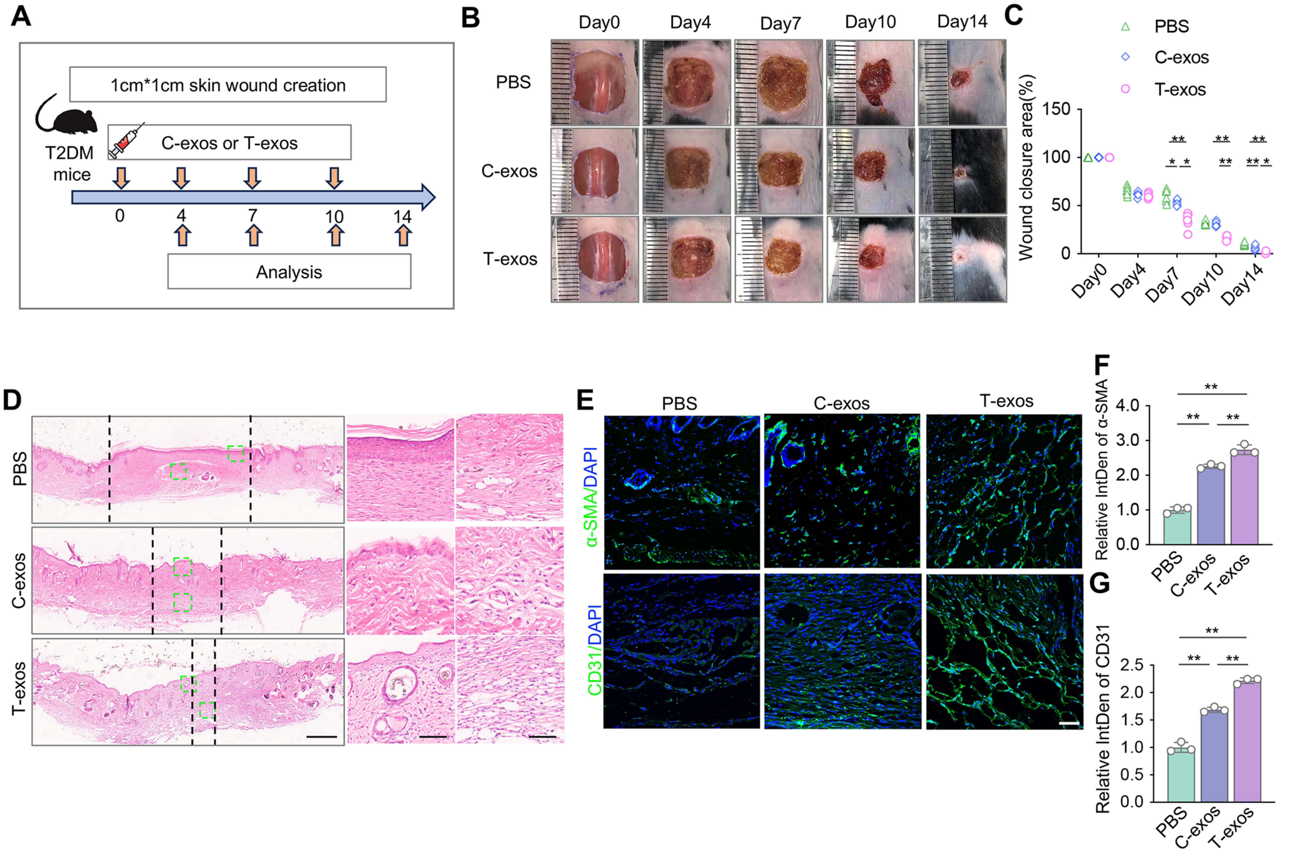

**Figure 4** T-exos promote skin wound healing via inhibiting DC activation in T2DM mice. (**A**) Scheme illustrating generation of skin wound and treatment with C-exos or T-exos. Full-thickness square wounds are made in the skin of T2DM mice, and exosomes are infused via local subcutaneous injection 1 day after wound creation. (**B** and **C**). Representative images and quantification of skin wound area in T2DM mice treated with the equal number of C-exos or T-exos. (**D**) Representative H&E staining images of wounds in three groups on day 14 after wound creation. The enlarged image showed new skin structures such as the epidermis and hair follicles. Scale bars, 600 μm (left column) and 150 μm (right column). (**E**–**G**) Immunofluorescence images and quantifications of relative IntDen of α-SMA and CD31 positive cells in 14 days skin. Scale bar, 50 μm. Data are presented as mean ± SD (n = 6). ns, not significant. $^{*}P < 0.05$, $^{**}P < 0.01$.

T-exos exhibited therapeutic effects compared to the PBS group. Although T-exos exhibited the most prominent therapeutic effects, no significant difference was observed between C-exos and T-exos groups (Figure S4C and D). These findings suggest T-exos promote wound healing universally but are particularly effective in counteracting diabetic pathologies.

## T-Exos Repress NLRP3 Inflammasome to Inhibit DC Activation

The activation of the NLRP3 inflammasome pathway is closely associated with proinflammatory functions, such as immune activation and proinflammatory factor releases.[36,37] The chronic hyperglycemic conditions in T2DM were reported to induce the activation of the NLRP3 inflammasome pathway and trigger immune dysfunction.[38,39] The colocalization of CD11c, cleaved-Caspase1, and IL-1β near the T2DM mice skin wounds was visualized by fluorescence microscopy, which indicated NLRP3 inflammasome pathway play roles in mediating DC immune responses during diabetic wound healing (Figure 5A). To explore the regulatory mechanism of DCs in high glucose conditions, we tested the relative level of NLRP3 inflammasome pathway in DCs cultured in standard medium and HG medium. It showed that DCs cultured by HG expressed a higher ROS activity and significantly increased mRNA expression of NLRP3 and IL-1β (Figure 5B–D). The protein expression related to NLRP3 inflammasome pathway also had an upregulated tendency in HG group (Figure 5E). Moreover, the DCs supernatant contained more proinflammatory factor IL-1β and IL-18 in HG conditions than DCs in standard conditions (Figure 5F). These results confirmed that HG conditions stimulate the activation of the NLRP3 inflammasome pathway in DCs. We further evaluated the expression of NLRP3 inflammasome

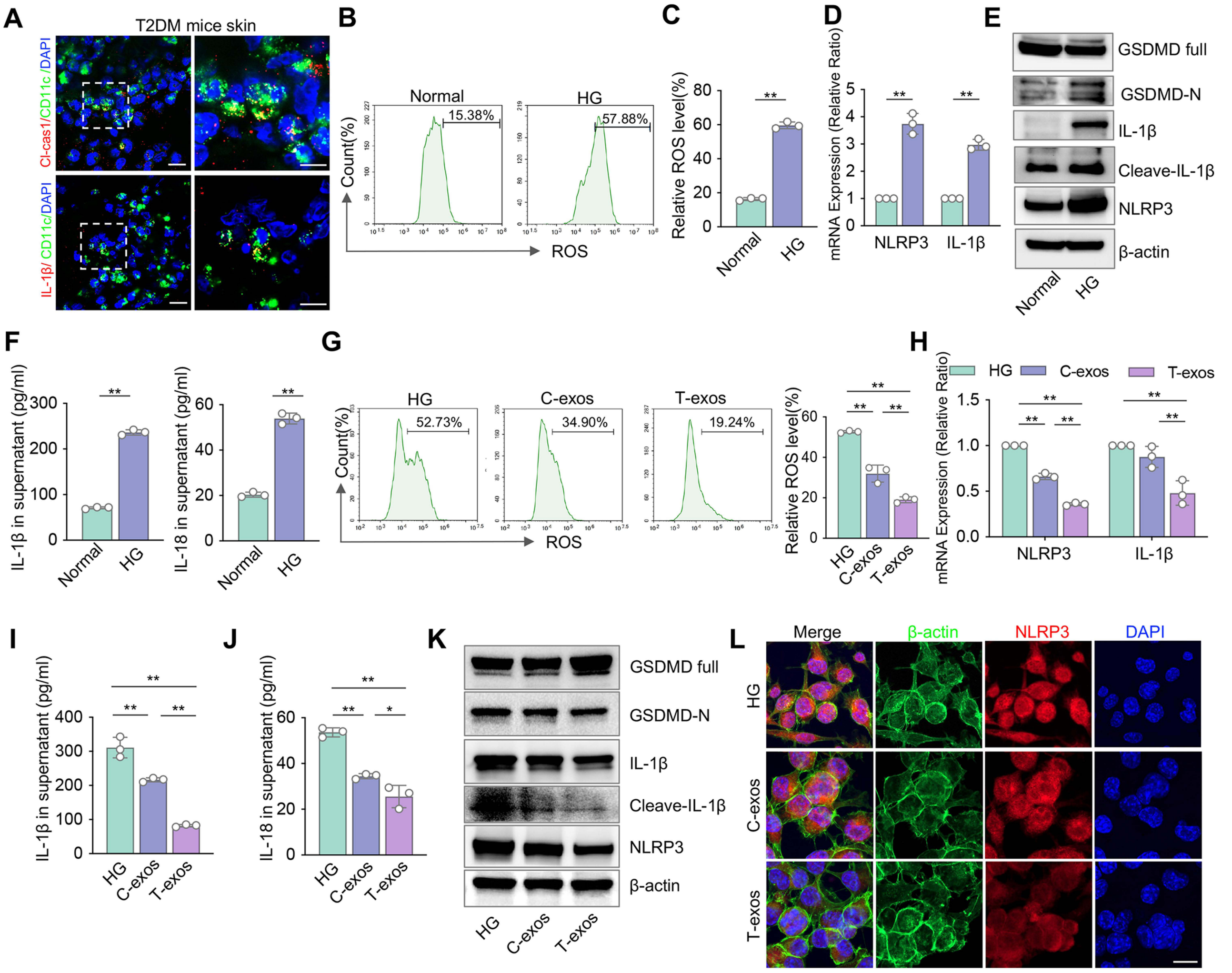

**Figure 5** T-exos impede DC activation by regulating NLRP3 inflammasome pathway. (**A**) The co-localization of CD11c and cl-cas1 (up) or IL-1β (down) in T2DM mice skin were visualized by fluorescence microscopy. Scale bar = 10 µm (left); 5µm (right). (**B** and **C**) The levels of ROS in DCs cultured in normal or HG medium were determined by flow cytometry analysis. (**D**) qRT-PCR analysis showed the mRNA levels of NLRP3 and IL-1β in DCs cultured by different conditions. (**E**) Western blots analysis showed the protein expression of normal-treated DCs and HG-treated DCs. (**F**) ELISA detected the secretion levels of IL-1β and IL-18 in normal and HG groups. (**G**) Flow cytometry analysis and quantification of ROS generation in DCs from HG, C-exos, and T-exos groups. (**H**) Relative gene expression levels of NLRP3 and IL-1β in HG, C-exos, and T-exos groups. (**I** and **J**) The secretion levels of IL-1β and IL-18 were detected by ELISA in three groups. (**K**) Western blots images of GSDMD full, GSDMD-N, IL-1β, Cleaved-IL-1β, NRLP3, and β-actin in HG, C-exos, and T-exos groups. (**L**) Immunofluorescence images revealed the expression of β-actin, NLRP3, and DAPI in DCs of different groups. Scale bar = 5 µm. Data are presented as mean ± SD (n = 3). ns, not significant. *$P < 0.05$, **$P < 0.01$.

pathway in DCs treated with different exosomes, to explore the potential mechanism clues of T-exos' immune modulatory effects. The flow cytometry assays indicated that ROS activity in DCs adhered to the sequence of HG > C-exos > T-exos (Figure 5G). qRT-PCR analysis showed that the T-exos group was significantly less than the other groups in mRNA expression of NLRP3 and IL-1β (Figure 5H). The ELISA assay demonstrated that DCs in the T-exos group exhibited diminished levels of the proinflammatory factor IL-1β and IL-18 compared to other groups (Figure 5I and J). The Western blot and immunofluorescence staining confirmed that the expression of typical proteins, including GSDMD, IL-1β, and NLRP3, were significantly deregulated in T-exos treated DCs (Figure 5K and L). Additionally, we inhibited the activation of the NLRP3 inflammasome utilizing MCC950, and found T-exos have equivalent effects as MCC950 in inhibiting the NLRP3 inflammasome pathway (Figure S5A–D). Then, we explored the immune status and NLRP3 inflammasome pathway of DCs in skin defect of T2DM mice. To investigate the targeting effect of exosomes on subcutaneous DCs in T2DM conditions, the PKH26 labeled exosomes derived from ADSCs were subcutaneous injection at the local skin of T2DM mice (Figure 6A). Immunofluorescent staining showed a relatively denser distribution of DCs

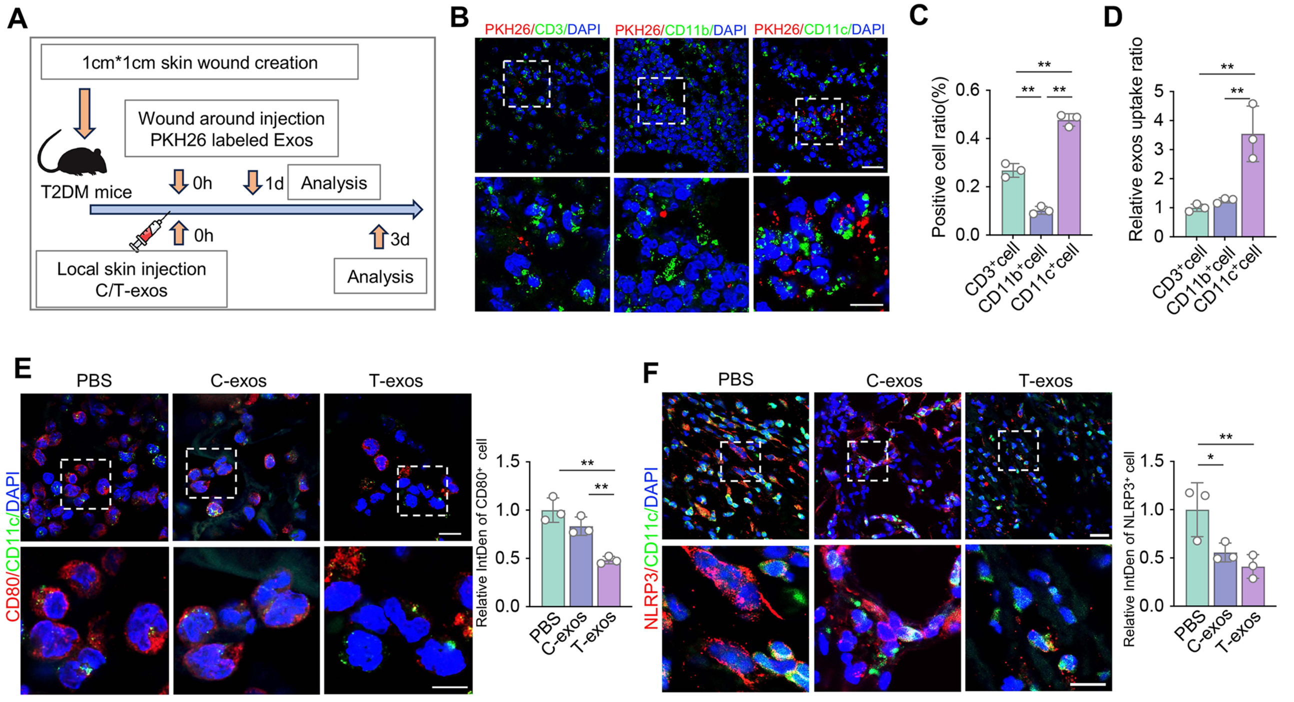

**Figure 6** T-exos inhibit DC activation by regulating NLRP3 inflammasome pathway in vivo skin defect of T2DM model. (**A**) PKH26 labeled exosomes tracing in T2DM mice skin schema and local skin injection C-exos/T-exos schema. (**B–D**) Immunofluorescent staining shows the uptake of PKH26-labeled exosomes by three types of immune cells. The quantification of relative proportions of immune cells and every immune cell uptake capacity of exosomes was calculated. CD3$^+$ cell, CD11b$^+$ cell, and CD11c$^+$ cell represent myeloid immune cells, macrophages, and dendritic cells, respectively. Scale bar = 10 µm (up), 5 µm (down). (**E**) The co-localization of CD11c-positive (green) and CD80-positive (red) cells in injured skin around after 3 days of injection of C-exos/ T-exos. Scale bar = 10 µm (up), 5 µm (down). The relative IntDen of CD11c and CD80 were analyzed by ImageJ. (**F**) Immunofluorescence images of CD11c, NLRP3, and DAPI expression near the wound at 3 days post injury. Scale bar = 10 µm (up), 5 µm (down). The relative IntDen of NLRP3 and CD11c were analyzed by ImageJ. Data are presented as mean ± SD (n = 3). ns, not significant. *$P < 0.05$, **$P < 0.01$.

in the skin compared to T cells and macrophages. Simultaneously, a larger number of exosomes were found to be targeted into DCs (Figure 6B–D). To explore the activation of DCs in vivo skin defect of T2DM mice, we detected the co-location of CD11c positive cells and CD80 positive cells in skin tissue at 3 days exosome injection. Immuno-fluorescence staining and relative integrated density quantification demonstrated that T-exos injection effectively inhibited DC activation in injured skin (Figure 6E). Additionally, immunofluorescence staining and relative integrated density quantification was conducted to detect NLRP3 level of DCs at 3 days post-wound creation, and the results showed less NLRP3 expression in CD11c-positive cells in T-exos group, while PBS group exhibited opposite tendency (Figure 6F). Overall, these findings suggest that T-exos inhibit DC activation by modulating the NLRP3 inflammasome pathway.

## T-Exos Regulate DC Activation Through miR-146a-5p/TXNIP/NLRP3 Axis

Next, we explored the underlying mechanisms through which T-exos regulate NLRP3 inflammasome in DCs. According to miRNA sequencing, 40 miRNAs were identified as being differentially expressed between C-exos and T-exos. Among them, 21 miRNAs were upregulated, and 19 miRNAs were downregulated in T-exos, compared with C-exos. The heatmap graph of expression levels showed the top 8 significantly changed miRNAs (Figure 7A). We noticed that the expression of miR-146a-5p was most significantly elevated in T-exos. The qRT-PCR results further confirmed that miR-146a-5p is highly expressed in T-exos compared to C-exos (Figure 7B). Next, we used the online database (Starbase) to explore the targets. Strikingly, bioinformatics analysis revealed that miR-146a-5p harbors multiple predicted binding sites with TXNIP, a key upstream regulator of the NLRP3 inflammasome pathway, and this direct interaction was experimentally validated via dual-luciferase reporter assays (Figures 7C, S6A and B). The Western blot further proved that TXNIP is lower expressed in T-exos treated DCs compared to C-exos treated DCs (Figure S6C). Therefore, T-exos possibly enriched miR-146a-5p to negatively regulate TXNIP and further downregulate NLRP3 inflammasome pathway. To examine our hypothesis, we transfected ADSCs with anti-miR-146a-5p, then collected miR-146a-5p-deficient

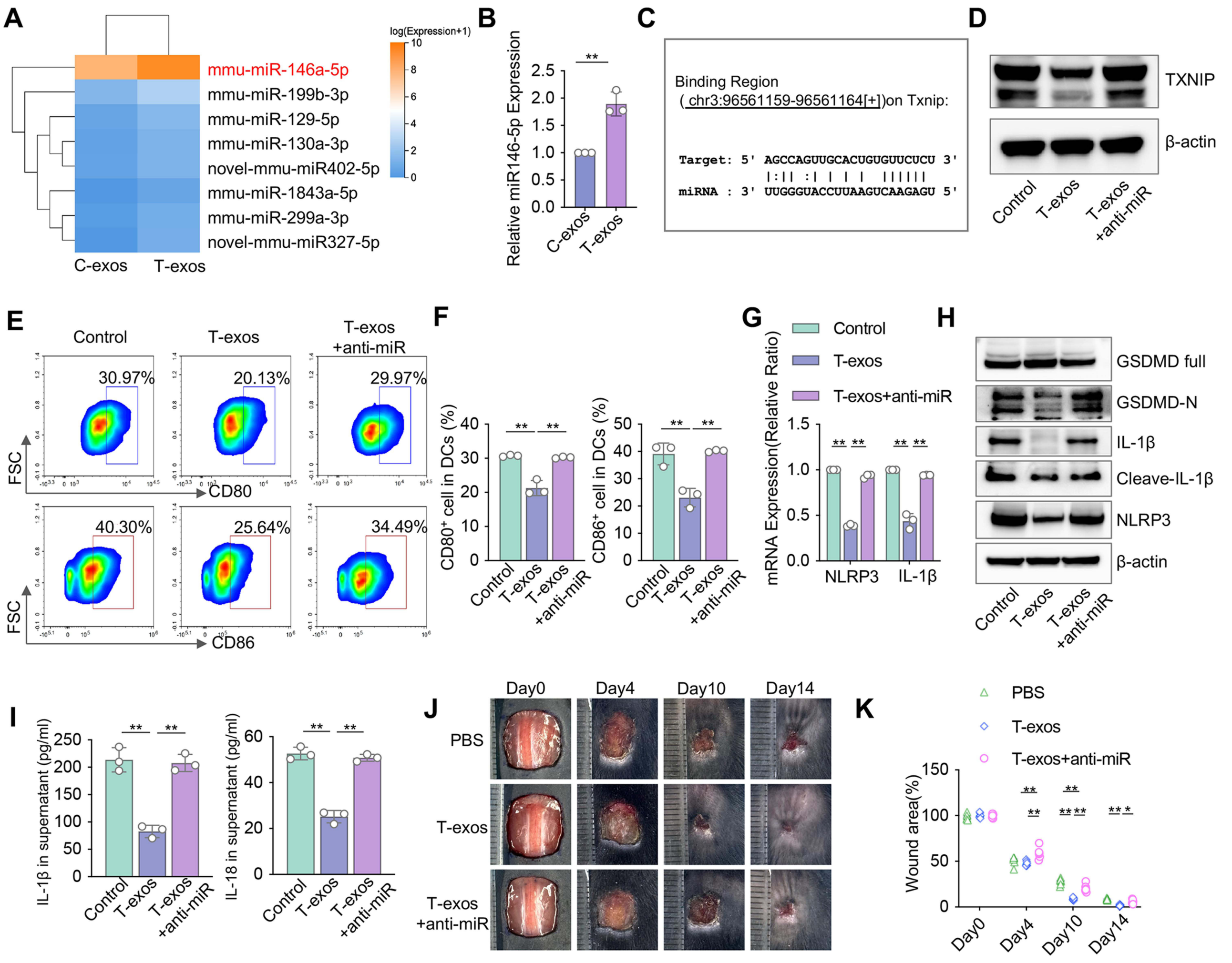

**Figure 7** T-exos inhibit DC activation and promote skin wound healing through miR-146a-5p/TXNIP/NLRP3 axis in T2DM mice. (**A**) Heatmap of differentially expressed miRNAs profiles (threshold fold change ≥1.5 and $p < 0.05$), with the 8 differentially expressed miRNAs shown. Hierarchical clustering of differentially expressed miRNAs (Fold change > 1.5 and Q value < 0.05) between C-exos and T-exos. The expression of miR-146a-5p was significantly upregulated. (**B**) The mRNA expression of miR-146a-5p was certified by qRT-PCR. (**C**) The predictive binding site between miR-146a-5p and TXNIP was from the online database. (**D**) An analysis of the target relationship for miR-146a-5p/TXNIP using Western blots in Controls, T-exos, and T-exos+anti-miR-146a-5p groups. (**E** and **F**) The flow cytometry analysis and quantity graph show relative expression levels of CD80 and CD86 in three groups. (**G**) The qRT-PCR analysis showed relative expression of NLRP3 and IL-1β. (**H**) Western blots analysis shows the expression levels of GSDMD full, GSDMD-N, IL-1β, Cleaved-IL-1β, NRLP3, and β-actin. (**I**) ELISA analysis indicates the levels of IL-1β and IL-18 in differently treated groups. (**J** and **K**) Representative macroscopic images and quantification of skin wound area in T2MD mice treated with PBS, T-exos, and T-exos treated by anti-miR-146a-5p. Cell data are presented as mean ± SD (n = 3), animal data are presented as mean ± SD (n = 6). ns, not significant. *$P < 0.05$, **$P < 0.01$.

exosomes from ADSCs to treat DCs. The Western blot showed that TXNIP of DCs increased after the knockdown of miR-146a-5p (Figure 7D). The flow cytometry, qRT-PCR, and Western blots further confirmed that the levels of DCs activation marker, as well as NLRP3 inflammasome pathway markers in anti-miR-146a-5p group, were similar with the HG group (Figures 7E–H, S6D and E). The flow cytometry results also suggested the increase of ROS in the T-exos +anti-miR group (Figure S6F, G). The ELISA results demonstrated that DCs in the T-exos+anti-miR group secreted elevated levels of the proinflammatory factor IL-1β and IL-18 compared to T-exos group (Figure 7I). To test the functions of miR-146a-5p in vivo, we injected differently treated exosomes around the wounds of T2DM mice. The images showed that wounds treated with T-exos closed faster than the other groups, while the wounds treated with T-exos transferred anti-miR-146a-5p healed slowly (Figure 7J and K). These results suggest that miR-146a-5p is the key effector in T-exos to regulate DC immune responses through the TXNIP/NLRP3 axis.

## Discussion

Immune dysfunction is a critical factor contributing to impaired tissue healing in the T2DM environment. Accumulating evidence indicates that TNF-α-preconditioned exosomes exhibit enhanced therapeutic efficacy in modulating immune homeostasis.[40,41] However, their involvement in facilitating diabetic wound repair and regulating DC functionality remains poorly characterized, particularly in the context of chronic hyperglycemia. In this study, we found the T-exos heightened therapeutic potency in restoring DC immune dysfunctions in T2DM conditions, which represents a significant advancement toward the clinical translation of MSC-exos. Our study innovatively explores the crucial role of T-exos in regulating DCs during wound healing in the T2DM context and dissects the detailed mechanisms underlying their effects.

Notably, immune cell dysfunction emerges as a hallmark feature, which subsequently impairs the functional capacities of fibroblasts and endothelial cells, ultimately compromising the wound healing process.[42,43] Although DCs have prominent functions in mediating inflammatory processes and immune cascades, less attention was focused on their roles during tissue regeneration yet.[44] In this study, we found abundant T-exos intake in DCs distributed in the skin, indicating that T-exos are ideal vehicles for treating phagocytes like DCs subcutaneously. Moreover, the results demonstrated that exosomes significantly promoted DC activation and proinflammatory cytokine secretion under both in vitro and in diabetic wounds. This excessive inflammation negatively impacted tissue-repairing cells, such as fibroblasts and endothelial cells, impairing wound closure. Importantly, our findings indicate that targeted modulation of DC function in T2DM conditions is a feasible therapeutic strategy to restore fibroblasts and endothelial cell behavior, promoting wound healing.

Host immune cells initiate a cascade of inflammatory responses through pattern recognition receptors (PRRs) upon stimulation by exogenous or endogenous signals.[45,46] The NLRP3 inflammasome is a multiprotein complex activated by hyperglycemia-derived reactive oxygen species (ROS) and thioredoxin-interacting protein (TXNIP).[31,47] Activation of NLRP3 inflammasomes triggers the proteolysis of caspase-1, leading to the maturation and release of proinflammatory factors, causing inflammation-related tissue damage.[48–50] However, the pathological changes of NLPR3 inflammasomes in DCs under T2DM conditions receive much less attention. In this study, we primarily explored that T2DM conditions trigger DC maturation through activating the NLRP3 inflammasomes pathway, and found that NLRP3 can act as an effective intervention target for DC immune responses in T2DM. According to a recent study, other than NLRP3 inflammasome, efferocytosis is vital in controlling DC works during wound healing. Therefore, it would be attractive and important to gain a thorough understanding of detailed DC actions in mediating tissue repair processes in the future.

Exosomes exert biological effects via loading diversity of cargos, including RNA, protein, and lipid.[51] miRNAs are enriched in exosomes and can regulate target cell behaviors via influencing mRNA translation and protein synthesis.[52–55] In this study, we explored the miRNA expression in T-exos by miRNA sequencing, revealing a significant upregulation of miR-146a-5p. Bioinformatics analysis and experimental validation identified TXNIP as a direct target of miR-146a-5p, a critical regulator upstream of the NLRP3 inflammasome pathway. This regulatory relationship was further confirmed by siRNA-mediated knockdown experiments. Therefore, we concluded that TNF-α preconditioning can not only improve the production of exosomes, but also increase the miRNA abundance inside exosomes, and form the miR-146a-5p/TXINP/NLRP3 axis, further regulating the NLRP3 inflammation pathway.

It is well established that immune regulation plays a crucial role for intervening in wound healing in T2DM. Existing studies mainly focus on reducing local inflammatory levels and promoting tissue regeneration in diabetic wounds by regulating local macrophage immunity, ROS scavenging, and other mechanisms.[6,7,56–58] However, a limitation of these studies lies in their neglect of the roles of other immune components in this process. This study clarifies the immune status characteristics of DCs in the T2DM environment and their impact on wound healing, providing another critical target for related therapeutic strategies. The clinical and economic value of MSC-exos are constrained by multiple factors, such as production yield and biological potency.[59] Compared with other stem cell therapies, pretreatment methods like TNF-α offer remarkable advantages in simplification and efficacy. Moreover, different pretreatment strategies can individually orchestrate the final biological functions of exosomes.[60] Thus, pretreatment technologies including TNF-α hold promise as pivotal approaches for the future clinical translation and industrialization of MSC-exos. In recent years, various biomaterials – including hydrogels - with exceptional biological properties and robust application potential have been widely applied in wound healing through controlled release and sustained antibacterial effects.[60–62] We hypothesize that integrating T-exos with sustained-release hydrogel carriers could facilitate the development of innovative therapies to accelerate diabetic wound healing. This strategy may also contribute to the advancement of novel diagnostic and therapeutic modalities for clinical challenges such as diabetic foot ulcers and diabetic periodontitis.

There were still some limitations in this study. Crosstalk between DCs and other immune cells plays an important role in wound healing,[63] which remains to be further clarified in T2DM. Moreover, the healing wound environment is complex, making it difficult to fully explain all physiological processes from a DC perspective. In addition, we need to learn more about the methods to enhance exosome function and specific miRNA. Exploring changes in exosomes from preconditioned MSCs could aid in developing efficient miRNA-engineered exosomes for future clinical use.

## Conclusion

This study elucidates a previously unrecognized role for T-exos in effectively regulating DC activation through the miR-146a-5p/TXINP/NLRP3 axis, which in turn modulates the NLRP3 inflammasome pathway. By synergistically dampening inflammation and enhancing tissue repair, T-exos exhibit significant potential for clinical application in T2DM wounds.

## Abbreviations

T2DM, type 2 diabetes mellitus; DCs, dendritic cells; MSC, mesenchymal stem cell; MSC-exos, mesenchymal stem cells-derived exosomes; T-exos, TNF-α-preconditioned MSC-exosomes; C-exos, untreated controls; ADSCs, adipose-derived MSCs; HG, high glucose; PBS, phosphate-buffered saline; TEM, transmission electronic microscopy; NTA, nanoparticle tracking analysis; H&E, hematoxylin and Eosin; qRT-PCR, quantitative real time PCR; Ct, cycle threshold; TBST, tris buffered saline with tween; BSA, bovine serum albumin; CCK-8, cell counting kit-8; ROS, reactive oxygen species; ELISA, enzyme-linked immunosorbent assay; CM, condition medium; T-CM, TNF-α-preconditioned condition medium; C-CM, untreated condition medium; PRRs, pattern recognition receptors; TXNIP, thioredoxin-interacting protein; WT, wild type txnip; Mut, mutant txnip.

## Data Sharing Statement

The data underlying this article will be shared on reasonable request by contact with the corresponding author.

## Compliance with Ethics Requirements

The animal studies were conducted following the protocols approved by the Institutional Animal Care and Use Committee at Sun Yat-sen University (SYSU-IACUC-2023-000078). The welfare and experimental procedures of laboratory animals adhered strictly to the "Animal management regulations of China" and "Guangdong experimental animal management regulations".

## Funding

This work was supported by grants from the National Natural Science Foundation of China (82170924 to X.K.).

## Disclosure

The authors declare no competing interests in this work.

## References

1. Saeedi P, Petersohn I, Salpea P, et al. Global and regional diabetes prevalence estimates for 2019 and projections for 2030 and 2045: results from the international diabetes federation diabetes atlas, 9(th) edition. *Diabet Res Clin Pract*. 2019;157:107843.
2. Ahmad E, Lim S, Lamptey R, et al. Type 2 diabetes. *Lancet*. 2022;400(10365):1803–1820. doi:10.1016/S0140-6736(22)01655-5
3. Liu YK, Ling S, Lui LMW, et al. Prevalence of type 2 diabetes mellitus, impaired fasting glucose, general obesity, and abdominal obesity in patients with bipolar disorder: a systematic review and meta-analysis. *J Affect Disord*. 2022;300:449–461. doi:10.1016/j.jad.2021.12.110
4. Rai V, Moellmer R, Agrawal DK. Stem cells and angiogenesis: implications and limitations in enhancing chronic diabetic foot ulcer healing. *Cells*. 2022;11(15):2287. doi:10.3390/cells11152287

5. Kalan LR, Meisel JS, Loesche MA, et al. Strain- and species-level variation in the microbiome of diabetic wounds is associated with clinical outcomes and therapeutic efficacy. *Cell Host Microbe*. 2019;25(5):641–55.e5. doi:10.1016/j.chom.2019.03.006
6. Wang Y, Chu T, Jin T, et al. Cascade reactions catalyzed by gold hybrid nanoparticles generate CO gas against periodontitis in diabetes. *Adv Sci*. 2024;11(24):2308587. doi:10.1002/advs.202308587
7. Qi X, Li Y, Xiang Y, et al. Hyperthermia-enhanced immunoregulation hydrogel for oxygenation and ROS neutralization in diabetic foot ulcers. *Cell Biomater*. 2025;1(3):100020. doi:10.1016/j.celbio.2025.100020
8. Wang M, Yao S, He D, et al. Type 2 diabetic mellitus inhibits skin renewal through inhibiting WNT-dependent Lgr5+ hair follicle stem cell activation in C57BL/6 mice. *J Diabetes Res*. 2022;2022:8938276. doi:10.1155/2022/8938276
9. Wang M, Lai Z, Zhang H, et al. Diabetes mellitus inhibits hair follicle regeneration by inducing macrophage reprogramming-mediated pyroptosis. *J Inflamm Res*. 2024;17:6781–6796. doi:10.2147/JIR.S469239
10. Sorg H, Tilkorn DJ, Hager S, et al. Skin wound healing: an update on the current knowledge and concepts. *Eur Surg Res*. 2017;58(1–2):81–94. doi:10.1159/000454919
11. Lee YS, Olefsky J. Chronic tissue inflammation and metabolic disease. *Genes Dev*. 2021;35(5–6):307–328. doi:10.1101/gad.346312.120
12. Zheng C, Sui B, Zhang X, et al. Apoptotic vesicles restore liver macrophage homeostasis to counteract type 2 diabetes. *J Extracell Vesicles*. 2021;10(7):e12109. doi:10.1002/jev2.12109
13. Aitcheson SM, Frentiu FD, Hurn SE, et al. Skin wound healing: normal macrophage function and macrophage dysfunction in diabetic wounds. *Molecules*. 2021;26(16):4917. doi:10.3390/molecules26164917
14. Clarkson BD, Heninger E, Harris MG, et al. Innate-adaptive crosstalk: how dendritic cells shape immune responses in the CNS. *Adv Exp Med Biol*. 2012;946:309–333.
15. Ronchese F, Hilligan KL, Mayer JU. Dendritic cells and the skin environment. *Curr Opin Immunol*. 2020;64:56–62. doi:10.1016/j.coi.2020.03.006
16. Haniffa M, Gunawan M, Jardine L. Human skin dendritic cells in health and disease. *J Dermatol Sci*. 2015;77(2):85–92. doi:10.1016/j.jdermsci.2014.08.012
17. Thomas AM, Dong Y, Beskid NM, et al. Brief exposure to hyperglycemia activates dendritic cells in vitro and in vivo. *J Cell Physiol*. 2020;235(6):5120–5129. doi:10.1002/jcp.29380
18. Rabelo MS, El-Awady A, Moura FA, et al. Influence of T2DM and prediabetes on blood DC subsets and function in subjects with periodontitis. *Oral Dis*. 2019;25(8):2020–2029. doi:10.1111/odi.13200
19. Burgess JL, Wyant WA, Abdo Abujamra B, et al. Diabetic Wound-Healing Science. *Medicina*. 2021;57(10):1072. doi:10.3390/medicina57101072
20. Clark GJ, Kupresanin F, Fromm PD, et al. New insights into the phenotype of human dendritic cell populations. *Clin Transl Immunol*. 2016;5(1):e61. doi:10.1038/cti.2015.40
21. Maschalidi S, Mehrotra P, Keceli BN, et al. Targeting SLC7A11 improves efferocytosis by dendritic cells and wound healing in diabetes. *Nature*. 2022;606(7915):776–784. doi:10.1038/s41586-022-04754-6
22. Henn D, Zhao D, Sivaraj D, et al. Cas9-mediated knockout of Ndrg2 enhances the regenerative potential of dendritic cells for wound healing. *Nat Commun*. 2023;14(1):4729. doi:10.1038/s41467-023-40519-z
23. Sun Y, Shi H, Yin S, et al. Human mesenchymal stem cell derived exosomes alleviate type 2 diabetes mellitus by reversing peripheral insulin resistance and relieving beta-cell destruction. *ACS Nano*. 2018;12(8):7613–7628. doi:10.1021/acsnano.7b07643
24. He Q, Wang L, Zhao R, et al. Mesenchymal stem cell-derived exosomes exert ameliorative effects in type 2 diabetes by improving hepatic glucose and lipid metabolism via enhancing autophagy. *Stem Cell Res Ther*. 2020;11(1):223. doi:10.1186/s13287-020-01731-6
25. Jiao Y-R, Chen K-X, Tang X, et al. Exosomes derived from mesenchymal stem cells in diabetes and diabetic complications. *Cell Death Dis*. 2024;15(4):271. doi:10.1038/s41419-024-06659-w
26. Brown C, McKee C, Bakshi S, et al. Mesenchymal stem cells: cell therapy and regeneration potential. *J Tissue Eng Regen Med*. 2019;13(9):1738–1755. doi:10.1002/term.2914
27. Xunian Z, Kalluri R. Biology and therapeutic potential of mesenchymal stem cell-derived exosomes. *Cancer Sci*. 2020;111(9):3100–3110. doi:10.1111/cas.14563
28. Zhang S, Chuah SJ, Lai RC, et al. MSC exosomes mediate cartilage repair by enhancing proliferation, attenuating apoptosis and modulating immune reactivity. *Biomaterials*. 2018;156:16–27. doi:10.1016/j.biomaterials.2017.11.028
29. Cheng J, Sun Y, Ma Y, et al. Engineering of MSC-derived exosomes: a promising cell-free therapy for osteoarthritis. *Membranes*. 2022;12(8):739. doi:10.3390/membranes12080739
30. Ying W, Riopel M, Bandyopadhyay G, et al. Adipose tissue macrophage-derived exosomal miRNAs can modulate in vivo and in vitro insulin sensitivity. *Cell*. 2017;171(2):372–84e12. doi:10.1016/j.cell.2017.08.035
31. Kang M, Huang CC, Gajendrareddy P, et al. Extracellular vesicles from TNFalpha preconditioned MSCs: effects on immunomodulation and bone regeneration. *Front Immunol*. 2022;13:878194. doi:10.3389/fimmu.2022.878194
32. Nakao Y, Fukuda T, Zhang Q, et al. Exosomes from TNF-alpha-treated human gingiva-derived MSCs enhance M2 macrophage polarization and inhibit periodontal bone loss. *Acta Biomater*. 2021;122:306–324. doi:10.1016/j.actbio.2020.12.046
33. Qin Y, Ge G, Yang P, et al. An update on adipose-derived stem cells for regenerative medicine: where challenge meets opportunity. *Adv Sci*. 2023;10(20):e2207334. doi:10.1002/advs.202207334
34. Long C, Wang J, Gan W, et al. Therapeutic potential of exosomes from adipose-derived stem cells in chronic wound healing. *Front Surg*. 2022;9:1030288. doi:10.3389/fsurg.2022.1030288
35. Chen H, Liu J, Shi GP, et al. Protocol for in vivo and ex vivo assessment of hyperglycemia and islet function in diabetic mice. *STAR Protoc*. 2023;4(1):102133. doi:10.1016/j.xpro.2023.102133
36. Blevins HM, Xu Y, Biby S, et al. The NLRP3 inflammasome pathway: a review of mechanisms and inhibitors for the treatment of inflammatory diseases. *Front Aging Neurosci*. 2022;14:879021. doi:10.3389/fnagi.2022.879021
37. He Y, Hara H, Nunez G. Mechanism and regulation of NLRP3 inflammasome activation. *Trends Biochem Sci*. 2016;41(12):1012–1021. doi:10.1016/j.tibs.2016.09.002
38. Ding S, Xu S, Ma Y, et al. Modulatory mechanisms of the NLRP3 inflammasomes in diabetes. *Biomolecules*. 2019;9(12):850. doi:10.3390/biom9120850

39. Lee HM, Kim JJ, Kim HJ, et al. Upregulated NLRP3 inflammasome activation in patients with type 2 diabetes. *Diabetes*. 2013;62(1):194–204. doi:10.2337/db12-0420
40. He X, Dong Z, Cao Y, et al. MSC-derived exosome promotes M2 polarization and enhances cutaneous wound healing. *Stem Cells Int*. 2019;2019:7132708. doi:10.1155/2019/7132708
41. Wang S, Wu R, Chen Q, et al. Exosomes derived from TNF-α-treated bone marrow mesenchymal stem cells ameliorate myocardial infarction injury in mice. *Organogenesis*. 2024;20(1):2356341. doi:10.1080/15476278.2024.2356341
42. Brem H, Tomic-Canic M. Cellular and molecular basis of wound healing in diabetes. *J Clin Invest*. 2007;117(5):1219–1222. doi:10.1172/JCI32169
43. Cheng S, Wang H, Pan X, et al. Dendritic hydrogels with robust inherent antibacterial properties for promoting bacteria-infected wound healing. *ACS Appl Mater Interfaces*. 2022;14(9):11144–11155. doi:10.1021/acsami.1c25014
44. Liu J, Zhang X, Cheng Y, et al. Dendritic cell migration in inflammation and immunity. *Cell Mol Immunol*. 2021;18(11):2461–2471. doi:10.1038/s41423-021-00726-4
45. Mathur A, Hayward JA, Man SM. Molecular mechanisms of inflammasome signaling. *J Leukoc Biol*. 2018;103(2):233–257. doi:10.1189/jlb.3MR0617-250R
46. Paik S, Kim JK, Silwal P, et al. An update on the regulatory mechanisms of NLRP3 inflammasome activation. *Cell Mol Immunol*. 2021;18(5):1141–1160. doi:10.1038/s41423-021-00670-3
47. Zhao Q, Liu G, Ding Q, et al. The ROS/TXNIP/NLRP3 pathway mediates LPS-induced microglial inflammatory response. *Cytokine*. 2024;181:156677. doi:10.1016/j.cyto.2024.156677
48. Cooke JP. Inflammation and its role in regeneration and repair. *Circ Res*. 2019;124(8):1166–1168. doi:10.1161/CIRCRESAHA.118.314669
49. Huang W, Jiao J, Liu J, et al. MFG-E8 accelerates wound healing in diabetes by regulating "NLRP3 inflammasome-neutrophil extracellular traps" axis. *Cell Death Discov*. 2020;6:84. doi:10.1038/s41420-020-00318-7
50. Huang Y, Xu W, Zhou R. NLRP3 inflammasome activation and cell death. *Cell Mol Immunol*. 2021;18(9):2114–2127. doi:10.1038/s41423-021-00740-6
51. Zhang Y, Bi J, Huang J, et al. Exosome: a review of its classification, isolation techniques, storage, diagnostic and targeted therapy applications. *Int J Nanomed*. 2020;15:6917–6934. doi:10.2147/IJN.S264498
52. Zhang J, Li S, Li L, et al. Exosome and exosomal microRNA: trafficking, sorting, and function. *Genomics Proteomics Bioinf*. 2015;13(1):17–24. doi:10.1016/j.gpb.2015.02.001
53. Nail HM, Chiu -C-C, Leung C-H, et al. Exosomal miRNA-mediated intercellular communications and immunomodulatory effects in tumor microenvironments. *J Biomed Sci*. 2023;30(1):69. doi:10.1186/s12929-023-00964-w
54. Zeng EZ, Chen I, Chen X, et al. Exosomal MicroRNAs as novel cell-free therapeutics in tissue engineering and regenerative medicine. *Biomedicines*. 2022;10(10):2485. doi:10.3390/biomedicines10102485
55. Li Q, Hu W, Huang Q, et al. MiR146a-loaded engineered exosomes released from silk fibroin patch promote diabetic wound healing by targeting IRAK1. *Sig Transduct Targeted Ther*. 2023;8(1):62. doi:10.1038/s41392-022-01263-w
56. Sharifiaghdam M, Shaabani E, Faridi-Majidi R, et al. Macrophages as a therapeutic target to promote diabetic wound healing. *Mol Ther*. 2022;30(9):2891–2908. doi:10.1016/j.ymthe.2022.07.016
57. Xiong Y, Chu X, Yu T, et al. Reactive oxygen species-scavenging nanosystems in the treatment of diabetic wounds. *Adv Healthcare Mater*. 2023;12(25):2300779. doi:10.1002/adhm.202300779
58. Patel S, Srivastava S, Singh MR, et al. Mechanistic insight into diabetic wounds: pathogenesis, molecular targets and treatment strategies to pace wound healing. *Biomed Pharmacother*. 2019;112:108615. doi:10.1016/j.biopha.2019.108615
59. Tan F, Li X, Wang Z, et al. Clinical applications of stem cell-derived exosomes. *Sig Transduct Targeted Ther*. 2024;9(1):17. doi:10.1038/s41392-023-01704-0
60. Chen S, Sun F, Qian H, et al. Preconditioning and engineering strategies for improving the efficacy of mesenchymal stem cell-derived exosomes in cell-free therapy. *Stem Cells Int*. 2022;2022:1779346. doi:10.1155/2022/1779346
61. Li H, Wen H, Zhang H, et al. A multifunctional Dihydromyricetin-loaded hydrogel for the sequential modulation of diabetic wound healing and Glycemic control. *Burns Trauma*. 2025;13. doi:10.1093/burnst/tkaf024
62. Wu S, Ge Y, Peng Y, et al. H 2 S/Curcumin coreleasing biomineralized zinc sulfide nanostructures for diabetic wound healing. *ACS Appl Nano Mater*. 2025;8(9):4749–4759. doi:10.1021/acsanm.4c07309
63. Knoedler S, Knoedler L, Kauke-Navarro M, et al. Regulatory T cells in skin regeneration and wound healing. *Mil Med Res*. 2023;10(1):49. doi:10.1186/s40779-023-00484-6